

THE FERMI-LAT GEV EXCESS TRACES STELLAR MASS IN THE GALACTIC BULGE

RICHARD BARTELS, EMMA STORM & CHRISTOPH WENIGER
GRAPPA, University of Amsterdam
Science Park 904, 1090GL Amsterdam, The Netherlands

FRANCESCA CALORE
LAPTh, CNRS
9 Chemin de Bellevue, 74941 Annecy-le-Vieux, France
(Received November 15, 2017; Revised; Accepted)

ABSTRACT

An anomalous emission component at energies of a few GeV and located towards the inner Galaxy is present in the *Fermi*-LAT data. It is known as the *Fermi*-LAT GeV excess. Using almost 8 years of data we reanalyze the characteristics of this excess with SKYFACT, a novel tool that combines image reconstruction with template fitting techniques. We find that an emission profile that traces stellar mass in the boxy and nuclear bulge provides the best description of the excess emission, providing strong circumstantial evidence that the excess is due to a stellar source population in the Galactic bulge. We find a luminosity to stellar mass ratio of $(2.1 \pm 0.2) \times 10^{27} \text{ erg s}^{-1} M_{\odot}^{-1}$ for the boxy bulge, and of $(1.4 \pm 0.6) \times 10^{27} \text{ erg s}^{-1} M_{\odot}^{-1}$ for the nuclear bulge. Stellar mass related templates are preferred over conventional DM profiles with high statistical significance.

1. INTRODUCTION

An anomalous emission component, often referred to as the Galactic center GeV excess (GCE), has been identified in the *Fermi*-LAT data by many groups (e.g. [Goodenough & Hooper 2009](#); [Vitale & Morselli 2009](#); [Hooper & Linden 2011](#); [Abazajian & Kaplinghat 2012](#); [Macias & Gordon 2014](#); [Daylan et al. 2016](#); [Zhou et al. 2015](#); [Calore et al. 2015b](#); [Huang et al. 2016](#); [de Boer et al. 2016](#); [Ajello et al. 2016](#)). Its spectrum peaks at energies of a few GeV and it appears to be uniform over the emission region. The morphology is usually described as almost spherically symmetric around the Galactic center, with a radial extent of $\sim 10^{\circ}$. Intriguingly, a signal from dark matter (DM) annihilation into b -quark pairs and a DM mass ~ 50 GeV has been shown to be consistent with the GCE ([Goodenough & Hooper 2009](#); [Abazajian & Kaplinghat 2012](#); [Macias & Gordon 2014](#); [Daylan et al. 2016](#); [Calore et al. 2015a](#)), provided the centrally peaked DM distribution in the Galactic bulge follows a radial power-law profile with index $\gamma \sim 1.2$. However, the exact details of the morphology and spectrum remain subject to debate, in particular due to the uncertainties in the interstellar emission modeling ([Carlson et al. 2016a](#); [Ackermann et al. 2017a](#)). Additionally, there is strong degeneracy with the *Fermi* Bubbles, giant diffuse lobes oriented perpendicularly to the Galactic plane ([Dobler](#)

[et al. 2010](#); [Su et al. 2010](#); [Ackermann et al. 2014](#)), the low-latitude behavior of which is not well-characterized ([Ackermann et al. 2017a](#); [Linden et al. 2016](#)).

Besides DM, more 'conventional' astrophysical explanations do exist, with various degrees of plausibility. These are either related to a large number of hitherto unresolved point sources in the Galactic bulge, just at and below the detection threshold of *Fermi*-LAT, or to diffuse photons coming from a central population of cosmic rays. Nowadays, a population of unresolved millisecond pulsars (MSPs), whose γ -ray spectrum was shown to match that of the GCE ([Abazajian 2011](#); [Abazajian et al. 2014](#); [Calore et al. 2015b](#)), represents the most promising astrophysical interpretation to the GCE ([Abazajian 2011](#); [Gordon & Macias 2013](#); [Petrović et al. 2015](#); [Yuan & Zhang 2014](#)). Corroborative evidence for this interpretation was recently found in analyses of the γ -ray data using wavelet fluctuations, and non-Poissonian template fits ([Bartels et al. 2016](#); [Lee et al. 2016](#)). Spectral classification of low-significance γ -ray sources and analyses of their distribution remain however inconclusive about the presence of a bulge population ([Ajello et al. 2017](#); [Bartels et al. 2017](#)). Lastly, it was recently shown that deep learning is another potentially powerful tool to discriminate between a point-source-like or diffuse-like structure of the excess ([Caron et al. 2017](#)). Although the evidence for the point source scenario is growing, it will require follow-up radio observations with MeerKAT and/or SKA to robustly confirm this interpretation ([Calore et al.](#)

2016), and exclude a DM interpretation for good.

Nevertheless, arguments against MSPs in the bulge exist and are based, for example, on the discrepancy between the required MSPs and the observed number of low-mass X-ray binaries progenitors (Haggard et al. 2017; Cholis et al. 2015) or on an implausibly high formation efficiency of MSPs in globular clusters (Hooper & Linden 2016). However, MSP evolutionary channels are complex and remain highly uncertain (Ploeg et al. 2017).

Surprisingly, possible connections between the morphology of the GCE and the morphology of the observed Galactic bulge received only little attention in the literature. The Milky Way hosts a central boxy/peanut-shaped bulge/bar that was likely formed from the buckling instability after the bar formation through bar instability (see e.g. Shen & Li 2016). The stellar mass of this boxy/peanut bulge, which is mostly made of old (>5 Gyr) stellar populations, is estimated to be $\sim 10^{10} M_{\odot}$, (e.g. Cao et al. 2013; Portail et al. 2017) about 15% of the total stellar mass in the Galaxy (McMillan 2011; Licquia & Newman 2015). The Galactic bulge has a radial extension of about 3 kpc and shows a complex morphological structure both in its stellar and gas content. It transitions into a thinner long bar component which extends about ~ 5 kpc (Wegg et al. 2015). In the innermost ~ 200 pc, we find the nuclear bulge (NB), a region of very high stellar density consisting of the nuclear stellar disk and the nuclear stellar (or star) cluster (Launhardt et al. 2002; Portail et al. 2017). In addition to the boxy/pseudo bulge, there exists evidence for the presence of a spherical classical bulge, revealed through metal-poor RR-Lyrae stars (Dékány et al. 2013; Kunder et al. 2016). This component is only expected to contribute 1% to the total mass in the inner-Galaxy, compared to $\sim 90\%$ for the boxy bulge (Kunder et al. 2016). Finally, there is evidence for an X-shaped component (McWilliam & Zoccali 2010; Nataf et al. 2010), which can naturally form from the buckling instability and, as such, is a product of bar evolution (Li & Shen 2012). Estimates of the mass of the X-shaped bulge range from a few percent of the total bulge mass (Li & Shen 2012; Cao et al. 2013) up to $\sim 45\%$ (Portail et al. 2015a). Recently, Macias et al. (2016) claimed that the GCE traces this X-shaped bulge and in the very center the nuclear bulge.

In the present paper, we analyze the GCE using our newly developed code SKYFACT (Sky Factorization with Adaptive Constrained Templates), Storm et al. 2017, which is a hybrid approach between template fitting and image reconstruction and allows for a much larger range of modeling systematics than previously possible. We compare the morphology of the GCE not only to DM-inspired models, but also to models that fit the stellar distribution in the inner Galaxy. The paper is

organized as follows: in Section 2 we describe our analysis methodology, using SKYFACT. Results are presented and discussed in Section 3, while we present our conclusions in Section 4. Full methods and a summary of SKYFACT are presented in Appendix A. In the supplemental material, Appendix B, we describe a number of systematics that could affect our results, including a detailed comparison of SKYFACT results and previous analyses, and the effects of the *Fermi* bubbles, additional point sources and star formation in the inner Galaxy.

2. MODELING THE γ -RAY SKY

We model the γ -ray sky using SKYFACT, a newly developed code for γ -ray data analysis that, through a combination of image reconstruction techniques and template fitting, accounts for expected spatial and spectral uncertainties in the various emission components by allowing a large number of ‘nuisance parameters’ (Storm et al. 2017). In this work, we adopt the data selection, foreground modeling, and regularization conditions as in RUN5 of Storm et al. (2017), unless stated otherwise. We perform fits in a region of interest (ROI) of $|\ell| \leq 90^{\circ}$ and $|b| \leq 20.25^{\circ}$, which is important for component separation, but we restrict most plots to $|\ell| \leq 20^{\circ}$ and $|b| \leq 20^{\circ}$ to highlight the region of the GCE.

In order to study the GCE, we model the GCE with fixed spatial templates and derive the energy spectrum from a fit to the γ -ray data. To this end, the following spatial templates are considered: (i) Templates inspired by annihilating DM: two generalized NFW templates with inner slopes of $\gamma = 1$ and $\gamma = 1.26$ (`r5_NFW100` and `r5_NFW126`) respectively and an Einasto profile with $\alpha = 0.17$ (`r5_Einasto`) (Navarro et al. 1997; Einasto 1965; Graham et al. 2006; Navarro et al. 2010); (ii) A superposition of two Gaussians and a Galactic central source used to model the 511 keV emission from the inner Galaxy by Siebert et al. (2016), `r5_BulgeGC`; (iii) Templates based on the stellar mass distribution in the Galactic bulge. We adopt a model for the boxy bulge derived from observations of red-clump giants, RCG (Cao et al. 2013). We also consider linear combinations of this model with the NB (`Launhardt et al. 2002`) and with the X-shaped bulge (`Ness & Lang 2016`). The addition of the latter is motivated by the recent results from Macias et al. (2016). These runs are labeled `r5_RCG`, `r5_RCG_NB` and `r5_RCG_NB.X`. For any linear combination the normalization of each component is left free to vary in each energy bin. Representative examples of these templates, along with the *Fermi*-LAT data, are illustrated in Fig. 1.

All of the runs above are also performed with a fixed MSP-like spectrum instead of a free spectrum (labeled with the suffix `_msp`). For these runs, we use the stacked MSP spectrum from McCann (2015), $dN/dE \propto E^{-1.46} \exp(-E/3.6)$. Fluxes and significances are de-

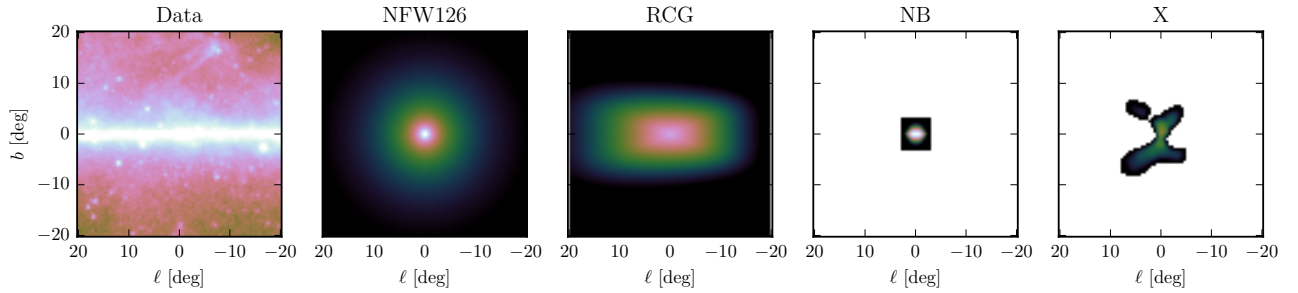


Figure 1: *Left panel:* *Fermi*-LAT data above 1 GeV in the inner $40^\circ \times 40^\circ$ around the Galactic center. *Other panels:* Spatial templates used to fit the GCE, with arbitrary normalization. From left to right: DM profile (NFW126), boxy-bulge, nuclear bulge, X-shaped bulge.

rived using the runs with fixed spectra.

We emphasize that, given the large modeling uncertainties of cosmic-ray induced γ -ray emission from the inner Galaxy, we do not explicitly include a source of cosmic rays at the GC when modeling the diffuse components. However, such sources are expected, *e.g.*, from star formation in the central molecular zone (CMZ, [Gaggero et al. 2015](#); [Carlson et al. 2016a,b](#)). The associated emission will depend on the efficiency of cosmic-ray acceleration, the effects of potentially strong advective winds or anisotropic diffusion, which are difficult to model in detail. In our analysis, the expected hard emission would be instead absorbed by our *Fermi* Bubbles component (see supplemental material, [B.4](#), for a discussion).

3. RESULTS AND DISCUSSIONS

3.1. Comparison of templates

Run	$-2 \ln \mathcal{L}$	
	free spectrum	MSP spectrum
r5_RCG_NB_X	647808.1	648020.2
r5_RCG_NB	647831.2	648027.5
r5_RCG	647884.7	648061.7
r5_BulgeGC	647916.5	648140.3
r5_Einasto	647961.4	648188.6
r5_NFW126	648021.8	648242.4
r5_NFW100	648049.8	648278.6

Table 1: Log-likelihood values for fits with various GCE templates. Column 2 shows results for a unconstrained GCE spectrum, and column 3 for a spectrum fixed to stacked MSPs.

In [Tab. 1](#) we compare the values of the total (Poisson plus constraints; see [Storm et al. \(2017\)](#) for details) log-likelihood, $-2 \ln \mathcal{L}$, from the SKYFACT runs, of the various modifications of RUN5 with different GCE templates with constrained morphology. We find that, formally, the combination of boxy bulge as traced by RCG and NB (r5_RCG_NB) provides a better fit to the data than

the other runs (except the one including the X-shaped bulge, see below). The total flux associated with the bulge is $(2.1 \pm 0.1) \times 10^{-9} \text{ erg cm}^{-2} \text{ s}^{-1}$ for the component traced by RCG and $(2.3 \pm 0.4) \times 10^{-10} \text{ erg cm}^{-2} \text{ s}^{-1}$ for the NB component (in the range 0.1–100 GeV). The quoted errors are statistical; we emphasize that typical systematic uncertainties from modeling assumptions (the range of allowed modulation parameters, etc.) are generally smaller than a factor ~ 2 .

We find that the addition of the X-shaped bulge can only mildly improve the fit quality. Its total flux is $(3 \pm 1)\%$ of that of the boxy bulge for the fixed spectrum run (r5_RCG_NB_X_msp). This value is only slightly smaller than the expectations from [Li & Shen \(2012\)](#) and [Cao et al. \(2013\)](#), who find the X-shape to be, by mass, about 6–7% of the boxy bulge (although fractions of 20–30% ([Portail et al. 2015b](#)) and $\sim 45\%$ ([Portail et al. 2015a](#)) have also been argued). We find that this component is not critical for providing a good fit to the data (2.7σ improvement), and will concentrate subsequently on the RCG+NB model. For a more detailed discussion of the X-shaped bulge and the from [Macias et al. \(2016\)](#) see the supplementary material [B.3](#).

We find that RCG+NB model provides a significantly better fit than any of the DM models. These DM profiles can be excluded with a high significance of about 12.5σ .

In [Fig. 2](#), we show the longitudinal and latitudinal dependences of the various model components compared with *Fermi*-LAT data, for two different GCE models, namely the r5_NFW126 and r5_RCG_NB runs. The solid lines correspond to the components of the r5_RCG_NB run, while the dashed lines of the same color correspond to the r5_NFW126 components, except for the GCE component, which is red (RCG) and orange (NB) for the r5_RCG_NB run and brown (NFW126) for the r5_NFW126 run. The dotted black and yellow lines are point sources and extended sources, respectively, which have the same total flux in both runs. There is very little variation in any components except those of the GCE (in the latitude profile, the extended source flux peaks just below

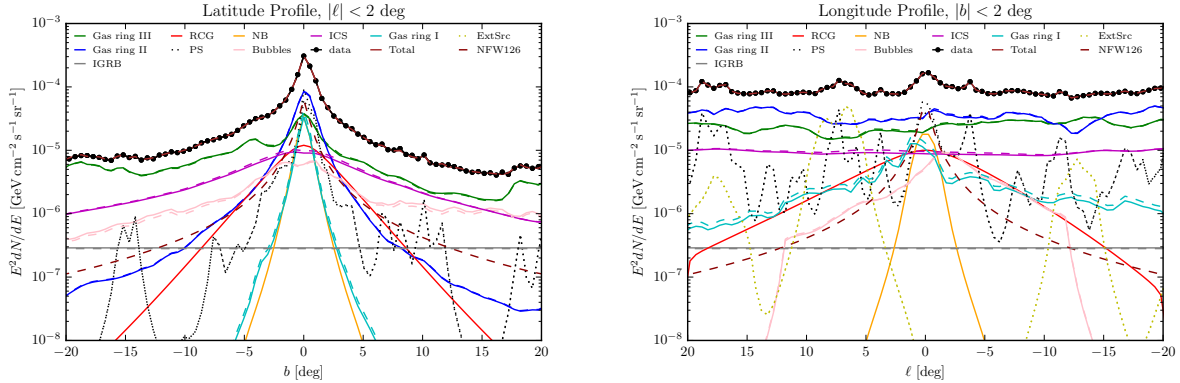


Figure 2: Measured flux compared to modeled flux as function of Galactic latitude (left panel, assuming $|\ell| < 2^\circ$) and longitude (right panel, assuming $|b| < 2^\circ$), for the best-fit run `r5.RCG_NB` (solid lines). The dashed lines show the best-fit fluxes obtained for run `r5.NFW126` for comparison. Dotted black and yellow lines represent the total point and extended source emission, respectively.

the lower limit of the plot). The shape differences between the RCG+NB templates compared to the NFW template are, however, quite large. The NFW is much more strongly peaked, and is of course spherically symmetric, while the oblateness and asymmetry of the RCG profile can be seen by comparing the shape of the tails in the latitude and the longitude profile plots.

In Fig. 3 on the left hand side, we show the spectra for all components of the `r5.RCG_NB` run in the inner $40^\circ \times 40^\circ$ around the Galactic center. On the right, we show the spectra for the RCG and NB components for separate runs where the spectral shape was left free to vary in one case and fixed to an MSP-like spectrum (with free overall normalization) in the other in the same region. The results from the free-spectra and fixed-spectra runs agree reasonably well, although the spectrum of the RCG component is somewhat more pronounced in the free-spectrum run. However, we find that the general preference for the RCG+NB scenario over DM-inspired templates is the same in both cases.

3.2. Light/mass ratios

We now estimate the light-to-mass ratio for the RCG and NB components separately. The stellar mass of the nuclear bulge is $(1.4 \pm 0.6) \times 10^9 M_\odot$ (Launhardt et al. 2002), while the mass of the boxy-bulge is $(0.91 \pm 0.7) \times 10^{10} M_\odot$ (Licquia & Newman 2015)¹.

Combining the mass measurements with the luminosities of the boxy-bulge and nuclear bulge components (mentioned above), the light-to-mass ratio for the bulge component is found to be $(2.1 \pm 0.2) \times 10^{27} \text{ erg s}^{-1} M_\odot^{-1}$,

¹ The bulge mass from Licquia & Newman (2015) is derived by combining bulge mass estimates from the literature in a hierarchical Bayesian analysis. We take this bulge mass as our reference value. However, we note that individual estimates range in best-fit value from $0.48 \times 10^{10} M_\odot$ to $2.74 \times 10^{10} M_\odot$, the range coming from different model assumptions and measurement techniques (see Licquia & Newman 2015, for a thorough discussion).

and for the NB component $(1.4 \pm 0.6) \times 10^{27} \text{ erg s}^{-1} M_\odot^{-1}$, from 0.1–100 GeV. The light/mass ratios of the two components are consistent within uncertainties, providing further circumstantial evidence that the GCE emission is correlated with stellar mass in the bulge.

The relation between stellar mass and the GCE luminosity is illustrated in Fig. 4. It shows the observed GCE intensity of various components compared to their stellar mass. This figure shows that, within uncertainties, the GCE emission indeed scales with stellar mass of the RCG and the NB component. Also shown is the excess of γ rays recently observed from the direction of M31, interpreted as a potential ‘‘GCE’’ in this galaxy (Ackermann et al. 2017b). We find that if this interpretation were correct, it would correspond to a larger emission per unit stellar mass by a factor ~ 4 than what is observed in the Milky Way (for details see the Methods section A.4).

Given that MSPs are the most likely candidate source class for the GCE, it is useful to quantify the corresponding emission expected from MSPs in the Galactic disk. We estimate the flux from the MSP disk population, using 3FGL γ -ray flux measurements of local MSPs (Acero et al. 2015) and distance and period information from the ATNF catalog (Manchester et al. 2005) (for details see supplementary material, Sect. A.3). From this, the expected bulge-to-disk flux (luminosity) ratio is $\sim 0.9(2.3)$ which implies a $\sim 10\times$ larger number of MSPs per unit of stellar mass in the bulge compared to the disk. Interestingly, this number is comparable to what is measured for another mysterious emission in the inner Galaxy, namely the 511 keV positron-annihilation-line emission (Knodlseder et al. 2005). This so-called 511 keV line emission has also been observed in the disk, with the latest estimate for the bulge-to-disk flux ratio being $B/D = 0.58 \pm 0.13$ (Siebert et al. 2016). We stress

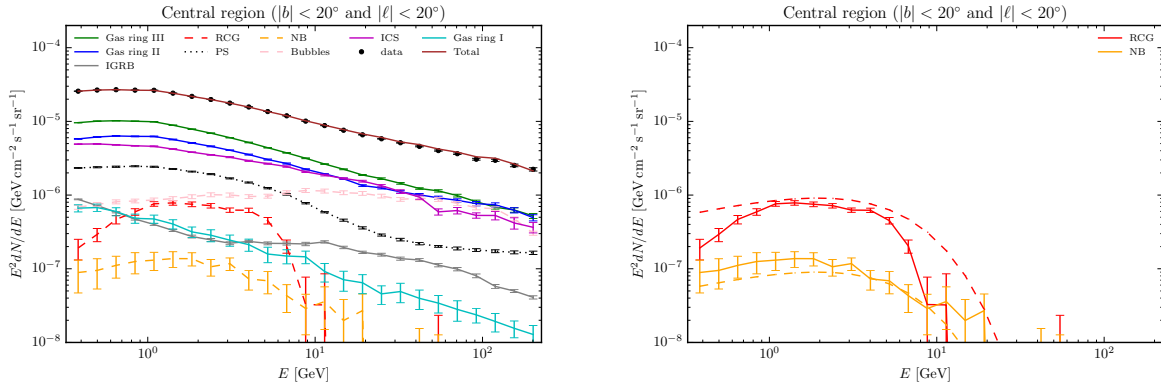


Figure 3: *Left panel:* Spectrum of the various model components in the region $|\ell|, |b| < 20^\circ$, as function of photon energy, for run `r5_RCG_NB`. *Right panel:* GCE spectra of RCG and NB component both for free spectra (solid) and for fixed spectra (dashed).

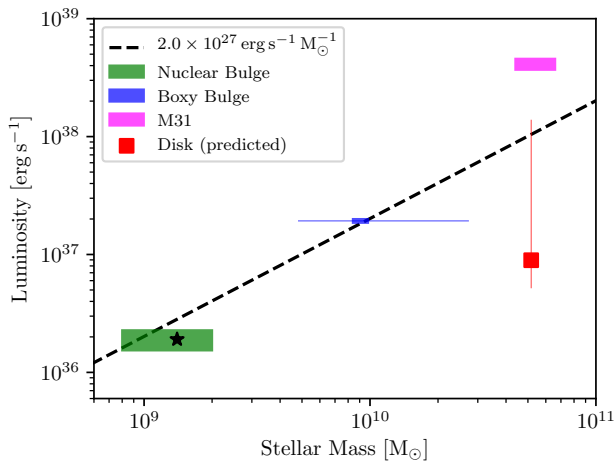


Figure 4: Stellar mass compared to the observed γ -ray luminosity for the boxy bulge (blue) and the nuclear bulge (green). Widths correspond to the uncertainty in the mass estimates, with the star indicating the best-fit mass of the NB (Launhardt et al. 2002). The boxy bulge mass comes is derived from a compilation of measurements into a hierarchical Bayesian analysis (box) the thin line displays the range of individual measurements (Licquia & Newman 2015). Heights reflect the uncertainty in the derived GCE flux. We also show the emission from M31 (Ackermann et al. 2017b) assuming that all γ -ray emission comes from its bulge, see methods Sect. A.4 for further details. The long-dashed line gives the relation of GCE emission per unit of stellar mass that best fits the combination of boxy bulge and nuclear bulge. Finally, the expected disk luminosity is shown as the red box. The estimate suffers from a large uncertainty due to the unknown γ -ray luminosity function, this uncertainty is bracketed by the thin red line.

however that the estimate for the MSP bulge-to-disk ratio is highly dependent on the assumed high-flux slope

of the MSP luminosity function, which is quite unconstrained (Strong 2007; Venter et al. 2014; Calore et al. 2014; Winter et al. 2016; Eckner et al. 2017). See Methods section A.3 for a more detailed discussion.

For the above estimate, the expected emission from MSPs in the disk is $\sim 8\%$ of the ICS flux and $\sim 2\%$ of the π^0 flux (in the 1-10 GeV band). Since the unresolved part of the disk MSP population makes up an even smaller fraction, we expect the corresponding diffuse contribution to be undetectable above the foregrounds and backgrounds.

3.3. Comparison with previous results

Previous analyses have typically found that the morphology of the GCE is spherically symmetric (Daylan et al. 2016; Calore et al. 2015b), although this is challenging to prove decisively mainly because of the contamination of the *Fermi* bubbles at low latitudes (Ackermann et al. 2017a). Additionally, some degree of elongation was found at high energies (Linden et al. 2016). Our findings are significantly different in this respect. We find that the critical difference between the previous and the current analyses is the inclusion of modulation parameters that account for uncertainties in the gas and ICS templates. The magnitude of these variations is completely expected, given the large uncertainties of the various templates (see the supplementary material B.1 for a detailed comparison). Our results are stable against variations of the regularization parameters (see supplementary material B.2 for a discussion).

4. CONCLUSION

We presented a novel analysis of the Galactic center GeV excess using the recently developed tool SKYFACT (Storm et al. 2017), allowing for the inclusion of a large number of nuisance parameters to take into account uncertainties in the foreground models. The effects of star

formation in the CMZ are not directly modeled, but associated hard emission is captured in the low-latitude part of our *Fermi* Bubbles component. We studied in detail the morphology of the GCE and we compared it against various templates, most notably the contracted NFW profile previously shown to describe the excess and a model that traces the stellar distribution of the bar/boxy bulge and nuclear bulge in the inner Galaxy.

We demonstrated that the stellar bulge model provides a significantly better fit ($> 10\sigma$) to the data than the DM-emission related Einasto or contracted NFW profiles. Hence the GCE appears to simply trace stellar mass in the bulge, not the dark matter density squared (although the actual DM profile is sufficiently uncertain that this possibility cannot be entirely excluded). What is more striking is that the light/mass ratio that we independently derive for the boxy bulge and the nuclear bulge are consistent with each other, supporting this interpretation.

The arguably best candidate sources are MSPs in the Galactic bulge. The putative bulge MSP population can be efficiently probed in the upcoming years with searches for radio pulsation signals (Calore et al. 2016) with MeerKAT or SKA. Our findings provide important information to guide these searches and strong motivation to perform them vigorously.

Acknowledgments— We thank Lia Athanassoula, David Berge, Gianfranco Bertone, Ilias Cholis, Roland Crocker, Oscar Macias, Pasquale Serpico, Tracy Slatyer, Andy Strong, Jacco Vink and Gabrijela Zaharijas for useful discussion. We acknowledge Daniele Gaggero for the support provided with the DRAGON code. RB would like to thank the organizers and participants of the TeVPA 2017 mini-workshop on the GCE for a fruitful discussion. This research is funded by NWO through the Vidi research program "Probing the Genesis of Dark Matter" (680-47-532; ES and CW), and through a GRAPPA-PhD fellowship (RB). FC acknowledges support from Agence Nationale de la Recherche under the contract ANR-15-IDEX-02, project "Unveiling the Galactic centre mystery", GCEM (PI: F. Calore).

REFERENCES

- Abazajian, K. N. 2011, JCAP, 1103, 010
 Abazajian, K. N., Canac, N., Horiuchi, S., & Kaplinghat, M. 2014, Phys. Rev., D90, 023526
 Abazajian, K. N., & Kaplinghat, M. 2012, Phys.Rev., D86, 083511
 Acero, F., et al. 2015, arXiv:1501.02003
 Ackermann, M., et al. 2012, ApJ, 750, 3
 Ackermann, M., et al. 2014, Astrophys. J., 793, 64
 Ackermann, M., et al. 2015, ApJ, 799, 86
 Ackermann, M., et al. 2017a, Astrophys. J., 840, 43
 —. 2017b, Astrophys. J., 836, 208
 Ajello, M., et al. 2016, Astrophys. J., 819, 44
 —. 2017, Submitted to: Astrophys. J., arXiv:1705.00009
 Bartels, R., Hooper, D., Linden, T., et al. 2017, arXiv:1710.10266
 Bartels, R., Krishnamurthy, S., & Weniger, C. 2016, Phys. Rev. Lett., 116, 051102, [Phys. Rev. Lett.116,051102(2016)]
 Bouchet, L., Roques, J.-P., & Jourdain, E. 2010, Astrophys. J., 720, 1772
 Byrd, R. H., Lu, P., Nocedal, J., & Zhu, C. 1995, SIAM Journal on Scientific Computing, 16, 1190
 Calore, F., Cholis, I., McCabe, C., & Weniger, C. 2015a, Phys. Rev., D91, 063003
 Calore, F., Cholis, I., & Weniger, C. 2015b, JCAP, 1503, 038
 Calore, F., Di Mauro, M., & Donato, F. 2014, Astrophys. J., 796, 1
 Calore, F., Di Mauro, M., Donato, F., Hessels, J. W. T., & Weniger, C. 2016, Astrophys. J., 827, 143
 Cao, L., Mao, S., Nataf, D., Rattenbury, N. J., & Gould, A. 2013, Mon. Not. Roy. Astron. Soc., 434, 595
 Carlson, E., Linden, T., & Profumo, S. 2016a, Phys. Rev., D94, 063504
 —. 2016b, Phys. Rev. Lett., 117, 111101
 Caron, S., Gmez-Vargas, G. A., Hendriks, L., & Ruiz de Austri, R. 2017, arXiv:1708.06706
 Cholis, I., Hooper, D., & Linden, T. 2015, Phys. Rev., D91, 083507, [Phys. Rev.D91,083507(2015)]
 Daylan, T., Finkbeiner, D. P., Hooper, D., et al. 2016, Phys. Dark Univ., 12, 1
 De Angelis, A., et al. 2016, arXiv:1611.02232
 de Boer, W., Gebauer, I., Neumann, A., & Biermann, P. L. 2016, arXiv:1610.08926
 Dékány, I., Minniti, D., Catelan, M., et al. 2013, Astrophys. J., 776, L19
 Di Bernardo, G., Evoli, C., Gaggero, D., Grasso, D., & Maccione, L. 2013, J. Cosmology Astropart. Phys., 3, 036
 Dobler, G., Finkbeiner, D. P., Cholis, I., Slatyer, T., & Weiner, N. 2010, ApJ, 717, 825
 Dwek, E., Arendt, R. G., Hauser, M. G., et al. 1995, Astrophys. J., 445, 716
 Eckner, C., Hou, X., Winter, M., et al. 2017, To Appear, arXiv:1711.XXXX
 Edwards, T. D. P., & Weniger, C. 2017, arXiv:1704.05458
 Einasto, J. 1965, Trudy Astrofizicheskogo Instituta Alma-Ata, 5, 87
 Evoli, C., Gaggero, D., Grasso, D., & Maccione, L. 2008, J. Cosmology Astropart. Phys., 10, 018
 —. 2012, Physical Review Letters, 108, 211102
 Ferrière, K. M. 2001, Reviews of Modern Physics, 73, 1031
 Gaggero, D., Taoso, M., Urbano, A., Valli, M., & Ullio, P. 2015, JCAP, 1512, 056
 Gillessen, S., Eisenhauer, F., Trippe, S., et al. 2009, Astrophys. J., 692, 1075
 Goodenough, L., & Hooper, D. 2009, arXiv:0910.2998
 Gordon, C., & Macias, O. 2013, Phys. Rev., D88, 083521, [Erratum: Phys. Rev.D89,no.4,049901(2014)]
 Graham, A. W., Merritt, D., Moore, B., Diemand, J., & Terzic, B. 2006, Astron. J., 132, 2685
 Haggard, D., Heinke, C., Hooper, D., & Linden, T. 2017, JCAP, 1705, 056
 Hooper, D., & Linden, T. 2011, Phys. Rev., D84, 123005
 —. 2016, JCAP, 1608, 018
 Huang, X., Enlin, T., & Selig, M. 2016, JCAP, 1604, 030
 Jouvin, L., Lemièrre, A., & Terrier, R. 2017, MNRAS, 467, 4622
 Knodlseder, J., et al. 2005, Astron. Astrophys., 441, 513
 Kunder, A., Rich, R. M., Koch, A., et al. 2016, ApJ, 821, L25
 Lang, D. 2014, AJ, 147, 108
 Launhardt, R., Zylka, R., & Mezger, P. G. 2002, Astron. Astrophys., 384, 112

- Lee, S. K., Lisanti, M., Safdi, B. R., Slatyer, T. R., & Xue, W. 2016, *Phys. Rev. Lett.*, 116, 051103, [Phys. Rev. Lett.116.051103(2016)]
- Levin, L., et al. 2013, *Mon. Not. Roy. Astron. Soc.*, 434, 1387
- Li, Z.-Y., & Shen, J. 2012, *Astrophys. J.*, 757, L7
- Licquia, T. C., & Newman, J. A. 2015, *Astrophys. J.*, 806, 96
- Linden, T., Rodd, N. L., Safdi, B. R., & Slatyer, T. R. 2016, *Phys. Rev.*, D94, 103013
- Lorimer, D. R. 2003, arXiv:astro-ph/0308501, [IAU Symp.218,105(2004)]
- Macias, O., & Gordon, C. 2014, *Phys.Rev.*, D89, 063515
- Macias, O., Gordon, C., Crocker, R. M., et al. 2016, arXiv:1611.06644
- Manchester, R. N., Hobbs, G. B., Teoh, A., & Hobbs, M. 2005, *Astron. J.*, 129, 1993
- McCann, A. 2015, *Astrophys. J.*, 804, 86
- McMillan, P. J. 2011, *Mon. Not. Roy. Astron. Soc.*, 414, 2446
- McWilliam, A., & Zoccali, M. 2010, *Astrophys. J.*, 724, 1491
- Morales, J. L., & Nocedal, J. 2011, *ACM Transactions on Mathematical Software (TOMS)*, 38, 7
- Nataf, D. M., Udalski, A., Gould, A., Fouque, P., & Stanek, K. Z. 2010, *Astrophys. J.*, 721, L28
- Nataf, D. M., et al. 2013, *Astrophys. J.*, 769, 88
- Navarro, J. F., Frenk, C. S., & White, S. D. M. 1997, *Astrophys. J.*, 490, 493
- Navarro, J. F., Ludlow, A., Springel, V., et al. 2010, *Mon. Not. Roy. Astron. Soc.*, 402, 21
- Ness, M., & Lang, D. 2016, *AJ*, 152, 14
- Petrović, J., Serpico, P. D., & Zaharijas, G. 2015, *JCAP*, 1502, 023
- Ploeg, H., Gordon, C., Crocker, R., & Macias, O. 2017, *JCAP*, 1708, 015
- Portail, M., Gerhard, O., Wegg, C., & Ness, M. 2017, *Mon. Not. Roy. Astron. Soc.*, 465, 1621
- Portail, M., Wegg, C., & Gerhard, O. 2015a, *MNRAS*, 450, L66
- Portail, M., Wegg, C., Gerhard, O., & Martinez-Valpuesta, I. 2015b, *MNRAS*, 448, 713
- Porter, T. A., & Strong, A. W. 2005, *International Cosmic Ray Conference*, 4, 77
- Read, J. I. 2014, *J. Phys.*, G41, 063101
- Serabyn, E., & Morris, M. 1996, *Nature*, 382, 602
- Shen, J., & Li, Z.-Y. 2016, *Galactic Bulges*, 418, 233
- Siegert, T., Diehl, R., Khachatryan, G., et al. 2016, *Astron. Astrophys.*, 586, A84
- Skinner, G., Diehl, R., Zhang, X. L., Bouchet, L., & Jean, P. 2014, in *Proceedings of the 10th INTEGRAL Workshop: A Synergistic View of the High-Energy Sky*. 15-19 September 2014. Annapolis, MD, USA. Published online at <https://pos.sissa.it/228/>.
- Storm, E., Weniger, C., & Calore, F. 2017, *JCAP*, 1708, 022
- Strong, A. W. 2007, *Astrophys. Space Sci.*, 309, 35
- Su, M., Slatyer, T. R., & Finkbeiner, D. P. 2010, *ApJ*, 724, 1044
- Su, M., Slatyer, T. R., & Finkbeiner, D. P. 2010, *Astrophys. J.*, 724, 1044
- Tamm, A., Tempel, E., Tenjes, P., Tihhonova, O., & Tuvikene, T. 2012, *Astron. Astrophys.*, 546, A4
- Venter, C., Johnson, T. J., Harding, A. K., & Grove, J. E. 2014, in *Proceedings, 58th Annual Conference of the South African Institute of Physics (SAIP 2013): Zululand, South Africa, July 8-12, 2013*, 385-390. <https://inspirehep.net/record/1325765/files/arXiv:1411.0559.pdf>
- Vitale, V., & Morselli, A. 2009, in *Fermi gamma-ray space telescope. Proceedings, 2nd Fermi Symposium, Washington, USA, November 2-5, 2009*. <https://inspirehep.net/record/840760/files/arXiv:0912.3828.pdf>
- Wegg, C., Gerhard, O., & Portail, M. 2015, *MNRAS*, 450, 4050
- Winter, M., Zaharijas, G., Bechtol, K., & Vandenbroucke, J. 2016, *Astrophys. J.*, 832, L6
- Yuan, Q., & Zhang, B. 2014, *JHEAp*, 3-4, 1
- Zhou, B., Liang, Y.-F., Huang, X., et al. 2015, *Phys. Rev.*, D91, 123010
- Zhu, C., Byrd, R., & Nocedal, J. 1997, L-BFGS-B: Algorithm 778, FORTRAN routines for large scale bound constrained optimization. *ACM Transactions on Mathematical Software*, Tech. rep.

APPENDIX

A. METHODS

A.1. GCE templates

A.1.1. Template construction

We construct various spatial models to study the morphology of the GCE. Below we provide some additional motivation for the various templates and describe their construction.

When we construct the template from the density profile, we perform a line-of-sight (l.o.s.) integral over the density profile.

$$\frac{d\Phi}{d\Omega} \propto \begin{cases} \int_{\text{l.o.s.}} ds \rho^2(r(s)) ds & \text{(DM)} \\ \int_{\text{l.o.s.}} ds \rho(r(s)) ds & \text{(Stars)} \end{cases} \quad (\text{A1})$$

Here the parameter s describes the los, $r(s)$ is the distance away from the Galactic center, ρ is the density, Φ the flux on earth and Ω the solid angle. For annihilating DM the emission traces the density squared. Furthermore, we define

the following coordinates centered on the GC:

$$x_{\text{GC}}(s, \ell, b) = R_{\odot} - s \cos(b) \cos(\ell), \quad (\text{A2})$$

$$y_{\text{GC}}(s, \ell, b) = s \cos(b) \sin(\ell), \quad (\text{A3})$$

$$z_{\text{GC}}(s, b) = s \sin(b), \quad (\text{A4})$$

where $R_{\odot} = 8.3 \text{ kpc}$ is the distance from the Sun to the GC (Gillessen et al. 2009), ℓ is Galactic longitude and b Galactic latitude. Note that the solar system lies along the x-axis. The Galactocentric radius is now given by $r = \sqrt{x_{\text{GC}}^2 + y_{\text{GC}}^2 + z_{\text{GC}}^2}$.

A.1.2. Templates considered

Positron annihilation signal / 511 keV line— The all-sky positron-annihilation signal has a strong component corresponding to the Galactic bulge (Knodlseder et al. 2005). Galactic positron emission can be described by a disk component and a bulge component. The latter is well described by a superposition of two Gaussians, the broad and narrow bulge components (Bouchet et al. 2010; Siegert et al. 2016). In addition, Siegert et al. (2016) finds evidence for the presence of a central component that is consistent with being a point source. We model the 511 keV bulge using the spatial profile and intensity as described in Tables 2 and 6 of Siegert et al. (2016). We include the central source component, the narrow and broad bulge and refer to this as **r5_BulgeGC**. For the bulge we assume that the narrow (broad) component contains 28% (72%) of the total bulge flux (Skinner et al. 2014).

Boxy bulge— We model the boxy, or pseudo, bulge using the distribution of RCGs (Nataf et al. 2013; Cao et al. 2013). The number density of RCGs is well fit by the triaxial $E\beta$ model (Dwek et al. 1995; Cao et al. 2013):

$$n_{E\beta} \propto K_0(r_s) \quad (\text{A5})$$

$$r_s = \left[\left[\left(\frac{x}{x_0} \right)^2 + \left(\frac{y}{y_0} \right)^2 \right]^2 + \left(\frac{z}{z_0} \right)^4 \right]^{\frac{1}{4}}, \quad (\text{A6})$$

with K_0 the modified Bessel function of the second kind and $x_0 = 0.67 \text{ kpc}$, $y_0 = 0.29 \text{ kpc}$ and $z_0 = 0.27 \text{ kpc}$ scale lengths. We use the best-fit parameters from Cao et al. (2013) for the E3 model. A larger set of parametric models to describe the triaxial structure of the bulge are given in Dwek et al. (1995).

In case of the boxy bulge it is important that it is rotated. In order to perform the line-of-sight integral we have to perform coordinate transformation $(x, y, z) \rightarrow (x_{\text{GC}}, y_{\text{GC}}, z_{\text{GC}})$. The rotation of the major axis (x) is around the z -axis and is $\theta = 29.4^\circ$ away from y_{GC} in the counterclockwise direction (Cao et al. 2013). So the conversion is given by $x = y_{\text{GC}} \cos \theta + x_{\text{GC}} \sin \theta$ and $y = x_{\text{GC}} \cos \theta - y_{\text{GC}} \sin \theta$.

Nuclear bulge— The Nuclear Bulge (NB) is a distinct component in the inner part of our $\lesssim 300 \text{ pc}$ of our Galaxy with ongoing star formation (Serabyn & Morris 1996). It consists out of two components, the nuclear stellar disk (NSD) and the nuclear stellar cluster (NSC) (Launhardt et al. 2002). We model these two components following Launhardt et al. (2002), who find a total mass for the NB of $(1.4 \pm 0.6) \times 10^9 M_{\odot}$. For the mass density of the NSC we use

$$\rho(r) = \begin{cases} \frac{\rho_{0,\text{NSC}}}{1 + \left(\frac{r}{r_0}\right)^2}, & r \leq 6 \text{ pc} \\ \frac{\rho_{1,\text{NSC}}}{1 + \left(\frac{r}{r_0}\right)^3}, & 6 \text{ pc} < r \leq 200 \text{ pc} \\ 0, & r > 200 \text{ pc}. \end{cases} \quad (\text{A7})$$

Here $\rho_{0,\text{NSC}} = 3.3 \times 10^6 M_{\odot} \text{ pc}^{-3}$ and $\rho_{1,\text{NSC}}$ is defined such that the profile is continuous at the break.

The NSD is modeled as a combination of an exponential disk with a scale height of 45 pc and a broken power law for the radius:

$$\rho(r) = \begin{cases} \rho_{0,\text{NSD}} \left(\frac{r}{1 \text{ pc}} \right)^{-0.1} e^{-\frac{|z|}{45 \text{ pc}}}, & r < 120 \text{ pc} \\ \rho_{1,\text{NSD}} \left(\frac{r}{1 \text{ pc}} \right)^{-3.5} e^{-\frac{|z|}{45 \text{ pc}}}, & 120 \text{ pc} \leq r < 220 \text{ pc} \\ \rho_{2,\text{NSD}} \left(\frac{r}{1 \text{ pc}} \right)^{-10} e^{-\frac{|z|}{45 \text{ pc}}}, & r \geq 220 \text{ pc}. \end{cases} \quad (\text{A8})$$

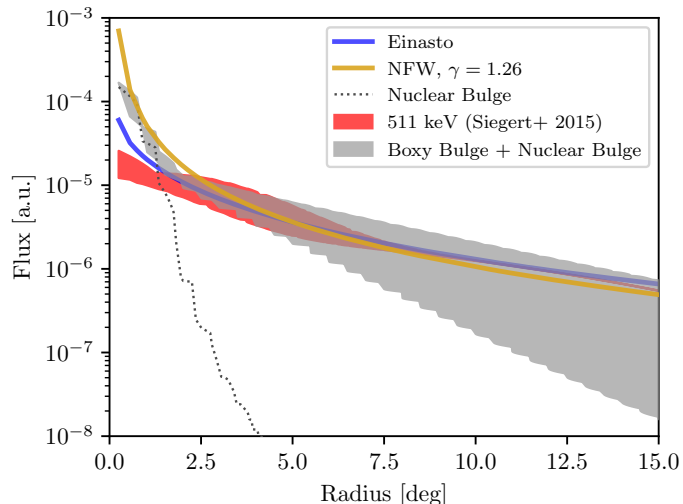


Figure A5:: Radial profiles for the various GCE templates considered in this analysis. All templates are smoothed with the *Fermi* Pass 8 ULTRACLEAN Front+Back angular resolution averaged between 1–10 GeV. The relative normalization between the NB and boxy bulge is determined by their total stellar masses $1.4 \times 10^9 M_\odot$ and $9.1 \times 10^{10} M_\odot$ respectively. Steps in the grey and red bands (line) are the result of the finite pixel size.

With $\rho_{0,\text{NSD}} = 301 M_\odot \text{pc}^{-3}$ such that the mass within 120 pc is $8 \times 10^8 M_\odot$. Again, $\rho_{1,\text{NSD}}$ and $\rho_{2,\text{NSD}}$ are defined such that the density profile is continuous.

X-shape— An X-shaped component is seen in the distribution of RCGs in the boxy bulge (McWilliam & Zoccali 2010; Nataf et al. 2010; Ness & Lang 2016). Such an X-shaped structure is a generic feature of pseudo bulges, believed to arise through the buckling instability (Li & Shen 2012).

We model the X-shaped bulge using the results from Ness & Lang (2016) and the public release of the WISE coadds (Lang 2014). We take the average of the residual maps in the W1 and W2 bands obtained using the public code² from Ness & Lang (2016), revealing the X-shaped structure. Any negative residuals are set to zero before averaging. This procedure is similar to that adopted by Macias et al. (2016).

DM profiles— We test two different classes of DM density profiles. First, we consider the NFW (Navarro et al. 1997; Graham et al. 2006) profile:

$$\rho(r) = \frac{\rho_s}{\left(\frac{r}{r_s}\right)^\gamma \left(1 + \frac{r}{r_s}\right)^{3-\gamma}}. \quad (\text{A9})$$

here γ defines the inner-slope, $r_s = 20$ kpc the scale-radius and ρ_s the scale density. We consider the common NFW profile with $\gamma = 1$ and a contracted NFW profile with $\gamma = 1.26$.

The second profile considered is the Einasto profile (Einasto 1965; Navarro et al. 2010):

$$\rho(r) = \rho_s \exp\left(-\frac{2}{\alpha} \left[\left(\frac{r}{r_s}\right)^\alpha - 1\right]\right). \quad (\text{A10})$$

Where we set $\alpha = 0.17$ and again we use $r_s = 20$ kpc.

Since we are only interested in the morphology the overall normalization is irrelevant, however, for completeness we mention that the density profile can be normalized using the DM density in the solar neighbourhood $\rho(R_\odot) = 0.4 \text{ GeV cm}^{-3}$ (Read 2014). Also note that the exact value of r_s is not very important, since this mostly affects the halo properties at large radii.

A.1.3. Template comparison

The radial profiles of the adopted spatial templates are compared in Fig. 5, where in case of a non-spherical template we show the *envelope* of the radial profile (for spherical templates, it is a single line). Templates are smoothed with the *Fermi* Pass 8 ULTRACLEAN Front+Back angular resolution averaged between 1–10 GeV. The spherically-symmetric DM profiles strongly peak towards the Galactic center. The 511 keV line emission model is less peaked towards

² Code available at <http://unwise.me>

the center and has a broader distribution, due to the small offset of one of the model components towards negative longitudes (Siegert et al. 2016). The combination of boxy bulge and nuclear bulge, weighted by their total stellar mass ($1.4 \times 10^9 M_\odot$ for the nuclear bulge and $0.91 \times 10^{10} M_\odot$ for the boxy bulge Launhardt et al. 2002; Licquia & Newman 2015) is also highly peaked towards the center because of the radial distribution of stars in the nuclear bulge. The stellar template follows the NFW profile out to almost $\sim 10^\circ$, but it has a much wider spread at larger radii due to its oblateness.

A.2. Analysis with SKYFACT

As mentioned in the main text, we use SKYFACT for fitting the γ -ray sky. We refer the reader to Storm et al. (2017) for a complete description of the approach. Here we briefly describe the approach to fitting, components used in modeling, and statistical analysis used in SKYFACT, highlighting any differences between this analysis and that in Storm et al. (2017).

A.2.1. Fits with SKYFACT

The main difference between fits with SKYFACT and more traditional template fitting is that SKYFACT allows for the introduction of nuisance parameters that can account for small, pixel-by-pixel variations and uncertainties in the spatial templates used in fitting. We model the diffuse flux in pixel p and energy bin b as the sum over k emission components,

$$\phi_{pb} = \sum_k T_p^{(k)} \tau_p^{(k)} \cdot S_b^{(k)} \sigma_b^{(k)} \cdot \nu^{(k)}, \quad (\text{A11})$$

where $T_p^{(k)}$ describes the morphology of emission component k , $S_b^{(k)}$ the model spectrum, and $\nu^{(k)}$ is an overall normalization. The parameters $\tau_p^{(k)}$ and $\sigma_b^{(k)}$ are, respectively, spatial and spectral modulation (or nuisance) parameters that account for uncertainties in the model morphology and model spectrum. These parameters are meant to vary around values of one, in a range that corresponds to our actual knowledge of the spectrum or morphology of each emission component. They are constrained to be non-negative to remain physically meaningful. The point source model is similar in structure, but without spatial templates or modulation parameters; see Storm et al. (2017) for the full model description.

We adopt a penalized likelihood approach, where the flexibility of the modulation parameters is controlled via regularization (or penalty) terms in the total likelihood function in the fit. The analytical structure of our regularization terms is motivated by the maximum-entropy method (MEM), as discussed in Storm et al. (2017). The diffuse flux is then multiplied by the exposure and convolved with the *Fermi* point spread function (PSF) to obtain the expected number of photons per pixel and energy bin. The predicted number of photons per bin are finally compared to the *Fermi* data using a Poisson likelihood.

Although the number of parameters in the above minimization (of $-2 \ln \mathcal{L}$) problem is very large, typically of the order of 10^5 , the minimization problem is, for reasonably constrained modulation parameters, convex and hence has a unique solution (Storm et al. 2017). We use the L-BFGS-B (Byrd et al. 1995; Zhu et al. 1997; Morales & Nocedal 2011) algorithm for this purpose, which makes use of analytical gradient information and implements the active set method to enforce non-negative boundaries on the fitting parameters. We estimate the uncertainties on fitted model parameters using the Hessian of the likelihood function, which we approximate by the inverse Fisher information matrix (as described in detail in Storm et al. (2017); see also Edwards & Weniger (2017)).

A.2.2. Data selection and model components

Data selection is identical to Storm et al. (2017): we use 7.6 years of Pass 8 ULTRACLEAN *Fermi* data binned into square pixels 0.5° on a side. Our foreground model consists of standard Galactic and extragalactic components: 1) hadronic emission from the π^0 decay produced by the interactions of cosmic ray protons with Galactic gas and dust, 2) ICS emission from cosmic ray electrons, 3) the extragalactic Isotropic Gamma-Ray Background (IGRB) emission, primarily the result of unresolved point sources, and 4) point sources and extended emission sources. We include an additional component that represents the *Fermi* Bubbles (Ackermann et al. 2014). Instead of the 511 keV template used for the GCE component in Storm et al. (2017), we here set up a variety of runs with different spatial templates for the GCE, detailed in Section 2.

As a tracer for the spatial distribution of π^0 decay γ -ray emission, we consider the sum of the atomic and molecular hydrogen column densities, assuming a constant conversion $X_{CO} = 1.9 \times 10^{20} \text{ cm}^{-2}/(\text{K cm/s})$. We build maps from those available in the GALPROP public release³. We split the gas templates in three radial bins: 0 – 3.5 kpc,

³ <https://galprop.stanford.edu/>

3.5 – 6.5 kpc and 6.5 – 19 kpc. For the three gas templates we impose a weak regularization on the morphologies (corresponding to variations within 32% for in the inner two rings and 50% for the outer ring), a weak regularization on the spectra starting from the ones measured in [Ackermann et al. \(2012\)](#) (within 25%), and a very weak smoothing. The normalization is instead completely unconstrained.

To compute the ICS template, we use the public code DRAGON ([Evoli et al. 2008](#)) and its custom companion GammaSKY ([Evoli et al. 2012](#); [Di Bernardo et al. 2013](#)). The ICS γ -ray emission model is built under standard assumption on the cosmic-ray source distribution ([Ferrière 2001](#)) and interstellar radiation field ([Porter & Strong 2005](#)), while we use propagation parameters corresponding to the “KRA4” model, see [Di Bernardo et al. \(2013\)](#). The ICS morphology is allowed to strongly vary (by a factor of 3). The ICS spectrum, as in the case of the hadronic template, is constrained to remain close to the spectrum measured in [Ackermann et al. \(2012\)](#) (within $\sim 25\%$). We do enforce a stronger smoothing than in the case of the gas, about 10% pixel-to-pixel variation. The overall normalization is again free to float.

We further include a template for the IGRB as measured in [Ackermann et al. \(2015\)](#). We allow its spectrum to slightly vary (within 25%) with respect to the spectrum derived from the diffuse background model A in [Ackermann et al. \(2015\)](#), while its normalization is fixed.

We add all 3FGL point sources within our ROI to the fit ([Acero et al. 2015](#)). We use a weak regularization on their spectra, allowing variations within 20%, while the overall normalizations are allowed to vary by 32%. We also consider 3FGL extended sources ([Acero et al. 2015](#)) within our ROI, weakly constraining the spectra and leaving the morphologies unconstrained (see details of the implementation in [Storm et al. 2017](#)).

As in [Storm et al. \(2017\)](#), we use a constrained (to within 5%) spectral template from [Ackermann et al. \(2014\)](#) with unconstrained spatial modulation allowed for the *Fermi* Bubbles component. In the supplementary information B, we discuss the effects of using alternative templates for this component.

The main technical difference between RUN5 in [Storm et al. \(2017\)](#) and this paper are the models used for the GCE. For each of the tested GCE components listed in the main text, the spatial modulation is fixed while the spectral modulation is set to be either essentially free (`r5_*`) or completely fixed to an MSP spectrum (`r5_*.msp`).

Lastly, we tested that a more complex version of the `r5_*` runs, where we split the CO and HI components of the outer ring and include a free template for the CMZ (which covers only the inner 4 pixels), does not affect the results significantly. Finally, we show in the supplementary material B that the impact of including the 2FIG catalog from [Ajello et al. \(2017\)](#) is minimal: the RCG+NB template is still preferred over the DM templates.

A.2.3. Statistical Analysis

The full likelihood used in SKYFACT is the sum of a standard Poisson likelihood and a regularization term that control the modulation parameters; a complete description is available in [Storm et al. \(2017\)](#). The full likelihood is used to calculate any significances listed in the paper.

For the comparisons between different GCE templates in Section 3 of the main text, we perform a standard likelihood ratio test using the full likelihood. We use only the runs with the fixed MSP spectra. For these runs, the difference in the degrees of freedom is simply equal to the the overall normalizations. When the spectra are left free, the difference in the degrees of freedom is less clear, due to the regularization. We describe a method to estimate the *effective* degrees of freedom with mock data in [Storm et al. \(2017\)](#), but for clarity, here we choose to compare the runs with the spectral degrees of freedom fixed (we also did this in [Storm et al. 2017](#) to estimate the significance of adding a GCE component). When comparing `r5_RCG_NB` and `r5_Einasto`, the difference in the degrees of freedom is 2, leading to the 12.5σ preference quoted in Section 3. This is the lowest significance of all the DM templates compared to the RCG+NB template. The preference for the RCG+NB template over the contracted NFW template, for example, is 14.5σ .

A.3. Estimating the bulge-to-disk flux ratio

A.3.1. Initial estimate

We estimate the bulge-to-disk ratio of GCE emission. First, we estimate the flux from detected MSPs within a local volume $D_{\odot} < 3$ kpc. To identify pulsars as belonging to the local volume and to be millisecond pulsars we compare all identified (PSR) and associated (psr) pulsars in the 3FGL ([Acero et al. 2015](#)) to their counterparts in the ATNF catalog ([Manchester et al. 2005](#)) and select those within 3 kpc from the Sun. Furthermore, we impose a cut at 30 ms on the pulsation period. In total we identify 47 γ -ray pulsars with periods below 30 ms in the local volume. The total flux from these sources is 1.2×10^{-9} (6×10^{-10}) $\text{erg cm}^{-2} \text{s}^{-1}$ from 0.1 – 100 GeV (from 1 – 10 GeV).

Next, we simulate a population of disk and bulge MSPs. For the spatial distribution in the disk we use a Lorimer disk

(Lorimer 2003), similar to Ajello et al. (2017). The radial distribution is $\rho(r) \propto r^{2.35} \exp(-r/1.528 \text{ kpc})$ and the height $\rho(z) \propto \exp(-|z|/z_0)$ where we set the scale height $z_0 = 0.5 \text{ kpc}$, Levin et al. (2013). Changing to $z_0 = 0.3 (0.7) \text{ kpc}$ increases (decreases) the disk flux by 10%. For the bulge we assume a spherically symmetric density profile that falls as $r^{-2.5}$ with a hard-cutoff at 3 kpc (Calore et al. 2015b). Final results are not expected to depend on the assumed bulge profile, since it is only used to compare the expected flux from a bulge source to that of a disk source, and for any bulge model the sources are located in the vicinity of the Galactic center.

We can obtain the disk flux from the local flux. Using the simulation we can estimate the number of sources in the local volume. The fraction of local MSPs compared to the full population is $f_{\text{local}} = 4.7\%$. In addition, we have to compare mean fluxes from the local volume, disk and bulge. For a given reference luminosity, L_0 , the mean flux can be calculated as

$$\langle S \rangle \propto \int ds \frac{dN}{ds} \frac{L_0}{s^2}, \quad (\text{A12})$$

where s is the distance along the line-of-sight and $\frac{dN}{ds}$ the distribution of sources along the line-of-sight, which we obtain from the simulation described earlier. The disk flux can now be calculated

$$S_{\text{disk}} = \frac{S_{\text{local}} \langle S \rangle_{\text{disk}}}{f_{\text{local}} \langle S \rangle_{\text{local}}}. \quad (\text{A13})$$

Using the derived bulge flux from this paper we naively estimate B/D flux ratio to be ~ 1.6 . Since the average bulge source is dimmer than the average disk source, the luminosity ratio is even larger, $B/D \sim 4.1$. Note that this estimate does not have a completeness correction for the disk.

A.3.2. Adjusting the estimate for completeness

In the above estimate we assumed that the flux from local MSPs is complete up to a distance of 3 kpc. In the following we estimate the completeness and modify our estimate accordingly. Ajello et al. (2017) argue that down to fluxes of $10^{-5} \text{ MeV cm}^{-2} \text{ s}^{-1}$ in the 0.3 – 500 GeV range the efficiency for a pulsar in the inner Galaxy to end up being classified as a pulsar candidate in the Second *Fermi* Inner Galaxy catalog (2FIG) is about 100%. This flux translates to $\sim 2 \times 10^{-11} \text{ erg cm}^{-2} \text{ s}^{-1}$ above 0.1 GeV. Conservatively, we estimate the local number pulsars to be complete down to $\sim 4 \times 10^{-11} \text{ erg cm}^{-2} \text{ s}^{-1}$. We find a total of 8 sources with a flux equal or larger than this value.

To estimate the total flux from the local volume we simulate a population of MSPs with a single power-law luminosity function: $dN/dL \propto L^{-1.5}$ from L_{min} to L_{max} , where $[L_{\text{min}}, L_{\text{max}}] = [10^{32}, 7 \times 10^{34}] \text{ erg s}^{-2}$ above 0.1 GeV. The slope is motivated by $L \propto \dot{E}^\beta$ where \dot{E} is the MSP spin-down power (Strong 2007). The slope, β , is uncertain but appears close to unity (Calore et al. 2014; Venter et al. 2014). Moreover, a bulge MSP population with this luminosity function has been shown to be able to explain the results from Bartels et al. (2016) for $L_{\text{max}} = 7 \times 10^{34} \text{ erg s}^{-2}$. Below we comment on the impact the assumed luminosity function can have on the estimate of the disk flux.

Setting the number of sources with $S \geq 4 \times 10^{-11} \text{ erg cm}^{-2} \text{ s}^{-1}$ equal to the observed number (8) we find a local flux of $\sim 2 \times 10^{-9} \text{ erg cm}^{-2} \text{ s}^{-1}$, almost a factor two larger than the flux obtained from the 3FGL. The total flux is only mildly dependent on the lower cutoff, L_{min} . Changing the slope of the luminosity function to $\alpha = 1.2 (1.8)$ decreases (increases) the flux by about 10%. However, for the softer slope the flux becomes more sensitive to L_{min} .

With these results we update our estimates for the bulge-to-disk ratio, taking into account completeness, to a flux ratio of $B/D \sim 0.9$ and a luminosity ratio of $B/D \sim 2.3$. This implies a $\sim 10\times$ higher number of MSPs per unit of stellar mass in the bulge compared to the disk (for a disk mass of $M_{\text{disk}} = 5.17 \times 10^{10} M_\odot$ Licquia & Newman 2015).

Importance of the luminosity function — We highlight the importance of the assumed luminosity function in the above estimate. Using the luminosity function of the form $dN/dL \propto L^{-1.5}$ results in the local flux being estimated to be complete to within a factor ~ 2 . The reasoning behind this is that for this luminosity function most of the flux comes from brightest sources, which are mostly resolved. However, a different luminosity function, such as the one used in Winter et al. (2016), can yield a disk flux which is larger by an order-of-magnitude. In this case, the number of MSPs in the disk and bulge, when weighted by stellar mass, becomes comparable (Eckner et al. 2017). The luminosity function assumed in Winter et al. (2016) is given by a broken power-law,

$$\frac{dN}{dL} \propto \begin{cases} L^{-1.45}, & L < L_b \\ L^{-2.86}, & L \geq L_b \end{cases}, \quad (\text{A14})$$

with the break at $L_b = 8.7 \times 10^{32} \text{ erg s}^{-1}$. In this case most of the flux is produced by sources with luminosities around the break, L_b . The slope before the break is again consistent with $L \propto \dot{E}$. However, the bright sources, which we

observe, are beyond the break and have a much steeper slope. A steeper slope could for instance be explained through a faster spin-down rate of the most luminous sources. Since sources before the break would still be largely unresolved, this implies we have only resolved the peak of the iceberg and that we should see many more sources with slightly increased sensitivity. If the luminosity function from Winter et al. (2016) represents the true luminosity function of MSPs the flux in the resolved local sources would only contain $\mathcal{O}(10\%)$ of the total local flux, meaning that the disk is expected to be much brighter. In this case, the disk and bulge would roughly have an equal number of MSPs per unit of stellar mass, an intriguing possibility which is studied in detail in (Eckner et al. 2017).

A.3.3. Comparing the emission from disk MSPs with ICS and gas emission

To estimate the detectability of the MSP disk population component we compare its flux to the flux expected from ICS (comparable to a thick disk) and π^0 emission (comparable to a thin disk). The fluxes from 1 – 10 GeV obtained for these components in the $4.5^\circ \times 180^\circ$ ROI (run `r5_RCG_NB`) are $7.8 \times 10^{-8} \text{ erg cm}^{-2} \text{ s}^{-1}$ (π^0) and $1.6 \times 10^{-8} \text{ erg cm}^{-2} \text{ s}^{-1}$. We consider the disk flux (including the completeness correction) within this ROI and compare to these backgrounds. The flux from MSPs in the disk in the 1-10 GeV band is $\sim 8\%$ of the ICS flux and $\sim 2\%$ of the π^0 flux. Since the estimate for the disk flux includes the resolved fraction, with sources in the local volume already making up $\sim 30\%$ of the total flux, the diffuse unresolved contribution will be an even smaller fraction. Consequently, the diffuse part of the GeV emission from disk MSPs falls well within the uncertainties of this emission components and it is unlikely to detect the disk as a separate component. However, we remind the reader that the estimate of the disk MSPs depends on the assumed luminosity function, in case of a luminosity function similar to that of Winter et al. (2016) the emission from disk MSPs becomes comparable to the ICS component.

In order to gauge the strength of the MSP disk γ -ray emission we performed a fit including a Lorimer disk as described above with the spectrum fixed to a stacked MSP spectrum. The normalization of this template remained close to zero (relative to other templates). Therefore, it appears no strong MSP component in the disk is required.

A.4. M31

Recently, Ackermann et al. (2017b) detected γ -ray emission from M31 with a flux of $(5.6 \pm 0.6) \times 10^{-12} \text{ erg cm}^{-2} \text{ s}^{-1}$ and found marginal evidence for spatial extension. Assuming M31 is similar to our Milky Way we can estimate the predicted emission from M31 using the relation between bulge stellar mass and the GeV emission. Taking the distance to M31 to be 785 kpc and the stellar mass of the bulge $M_{\text{M31}} = (4.4 - 6.6) \times 10^{10} M_\odot$ (Tamm et al. 2012) we estimate that the luminosity of M31 to be $\sim 20\times$ that of the Milky Way bulge. Thus, assuming M31 is a Milky Way analog and that its γ -ray emission comes from the bulge it would have $\sim 4\times$ more MSPs per unit of stellar mass. Eckner et al. (2017) arrive at the same conclusion, albeit through a different analysis in which they start from an estimation of the number of MSPs in the disk.

Assuming a similar ratios of GeV emission per unit stellar mass in the bulge and disk of M31 as in those of the Milky Way, we estimate that $\sim 90\%$ of the potential GCE flux from M31 should come from the bulge and the remaining $\sim 10\%$ from the disk. Note that for the luminosity function where the majority of the flux is produced by sources of intermediate luminosity, such as that of Winter et al. (2016), the disk of M31 can become equally bright, or slightly brighter than the bulge, since in this case we expect the disk and bulge to have a similar amount of MSPs per unit of stellar mass. Eckner et al. (2017) show that in this case MSP emission from the disk is only just below the detection threshold. We note that the radius of the bulge in M31 is only $\sim 0.1^\circ$ (Tamm et al. 2012). Consequently, the observed bulge emission of 0.4° radius fit by a uniform brightness disk from Ackermann et al. (2017b) appears large. Future instruments with better spatial resolution (e.g. e-ASTROGAM or AMEGO⁴ De Angelis et al. 2016) could potentially better resolve the bulge (also see Eckner et al. (2017)).

B. SUPPLEMENTARY INFORMATION

B.1. Overview of runs and SKYFACT compared to traditional analyses

Tab. 2 shows an overview of all SKYFACT runs performed for this analysis. Runs starting with `r5_` are extensions or modifications of RUN5 from Storm et al. (2017). In Fig. 6, we show the best-fit spectra for the GCE components of all runs starting with `r5_` in Tab. 2. For these runs, the recovered spectra are quite similar, with less than 30% variation in peak flux. The spectrum of the X-shaped template is not well-recovered, since it is such a sub-dominant component; the error bars are also large on this component.

Runs starting with A–H in Tab. 2 connect the analysis of Calore et al. (2015b) to RUN5. We used the latter to

⁴ <https://asd.gsfc.nasa.gov/amego/index.html>

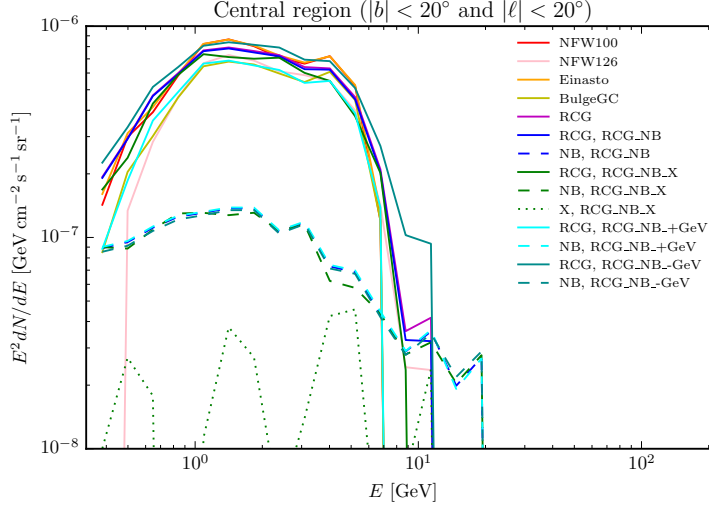


Figure B6:: Recovered spectra for the GCE component of all runs in Tab. 3 starting with `r5`. If there are multiple GCE components in a single run (e.g., the RCG+NB template), the two components are plotted separately. Error bars not shown for clarity.

identify how the current analysis differs from the previous results obtained with regular template fitting. To this end we changed the analysis assumptions step-by-step until we well reproduce the results from Calore et al. (2015b).

In this section we elaborate on the runs A1/A2–H1/H2 as listed in Tab. 2. When referring to the runs we will now drop the appended digit, and just mention that each runs was performed twice, ones for the NFW (1) and ones for the bulge template (2). The NFW template that is used has an inner slope of $\gamma = 1.26$ as in run `r5_NFW126` and the bulge template includes the boxy bulge as traced by red clump giants and the nuclear bulge, as in `r5_RCG_NB`. Note that the NB is fully masked when the disk is masked.

Run A mostly reproduces Model F from Calore et al. (2015b). It uses a smaller, $40^\circ \times 40^\circ$ ROI, the GALPROP gas and ICS templates from Model F, a uniform spatial bubble template (Su et al. 2010) and the Galactic disk is masked $|b| \geq 2^\circ$. The main difference is the point source treatment: runs A--H include all the 3FGL sources in the fit with free normalizations (same constraints as `run5` in Storm et al. 2017), whereas Calore et al. (2015b) mask point sources. For this run, the NFW template is preferred over the bulge template. We show the difference in fit quality, $\Delta\chi^2$, between the the NFW and bulge runs in Tab. 3. Step-by-step we release the constraints until we reproduce RUN5. In model B we change the gas and ICS templates to the ones used in RUN5; however, rather than using 3 rings for the π_0 template only a single template is used. Changing the gas template does not affect the preference for the NFW template. Run C extends the ROI to include the full latitude range used in the rest of this work, $|l| \leq 90^\circ$. The NFW profile still is preferred.

The largest change in the $\Delta\chi^2$ occurs between run C and D, where modulation parameters for the spatial templates are switched on. The NFW template is still formally preferred, but the difference is drastically reduced. If only the Poisson term of the likelihood is considered, the switch in preference for NFW to RCG+NB actually occurs here between runs C and D, but the regularization term in run D is large enough so that for the total likelihood, the NFW template is still preferred. Unmasking the disk in run E results in an overall preference for the RCG+NB template over the NFW. Next, the π_0 template is broken up into two rings in run F. Extended sources are added in run G. There is still a preference for the bulge template. Finally, we change the template for the bubbles from a uniform spatial template to a spectral template and thus recover RUN5 in H. Run H1 (H2) is identical to `r5_NFW` (`r5_RCG_NB`) except that the latter uses 3 gas rings. The choice of 2 or 3 gas rings does not affect the fit to the GCE.

B.2. Relevance of modulation parameter ranges

A critical component of the analysis, and in fact part of the reason why we obtain qualitatively different results than previous studies, is the inclusion of nuisance parameters in the various model templates. We here briefly summarize the main assumptions on the nuisance parameters that we made for our reference model. Full details can be found in Storm et al. (2017). Variations at the levels smaller than or equal to the constraints described above would be not surprising, and are of the size of actual residuals that one can find in standard template analyses.

Run ID	Comment
r5_NFW126	Bulge spectrum from spatial DM template
r5_NFW100	Bulge spectrum from spatial DM template
r5_Einasto	Bulge spectrum from spatial DM template
r5_BulgeGC	Bulge spectrum from spatial 511 keV template
r5_RCG	Bulge spectrum from spatial stellar mass template
r5_RCG_NB	Bulge spectrum from spatial stellar mass template; two components
r5_RCG_NB_X	Bulge spectrum from spatial stellar mass template; three components
r5_RCG_NB_+GeV	Softer Fermi bubble spectrum
r5_RCG_NB_-GeV	Harder Fermi bubble spectrum
r5_RCG_NB_pICS	Additional inner Galaxy ICS component with soft spectrum
r5_RCG_NB_pICS2	Additional inner Galaxy ICS component with hard spectrum
A1	Reproduction of Calore et al. (2015b), with spatial DM template.
A2	Reproduction of Calore et al. (2015b), with spatial stellar mass template.
B1	A1 gas/ICS templates changed to RUN5 templates (1 gas template).
B2	A2 gas/ICS templates changed to RUN5 templates (1 gas template).
C1	B1 with longitude extended to $ l \leq 90^\circ$.
C2	B2 with longitude extended to $ l \leq 90^\circ$.
D1	C1 with modulation as in RUN5.
D2	C2 with modulation as in RUN5.
E1	D1 with disk unmasked
E2	D2 with disk unmasked
F1	E1 with two gas rings used.
F2	E2 with two gas rings used.
G1	F1 with extended sources added in.
G2	F2 with extended sources added in.
H1	G1 with spectral bubble template.
H2	G2 with spectral bubble template.

Table B2:: Overview of different runs that we used in the present paper. All runs starting with `r5_` are extensions or modifications of `run5` from Storm et al. (2017), where more details about the background modeling can be found. `r5_` runs are also performed with the spectrum fixed to that obtained by McCann (2015) for stacked MSPs, in which case we append `_msp` to the run ID. Runs starting with A–H connect the analysis of Calore et al. (2015b) to RUN5. The only difference between RUN5 and H is that the gas template is broken up into 3 ring in the former and 2 in the latter.

Template	$-2 \ln \mathcal{L}$		$\Delta\chi^2$
	(1) NFW $\gamma = 1.26$	(2) RCG_NB	
A	147174.1	147486.0	-311.9
B	165359.2	167419.6	-2060.4
C	718013.4	721344.0	-3330.6
D	562568.4	562995.2	-426.8
E	655669.2	654782.6	886.6
F	655113.2	654947.4	165.8
G	651279.8	651022.9	256.9
H	648635.9	648484.5	151.4

Table B3:: $-2 \ln \mathcal{L}$ values for the various runs connecting Calore et al. (2015b) to RUN5. $\Delta\chi^2 = -2(\ln \mathcal{L}_{\text{NFW}} - \ln \mathcal{L}_{\text{RCG_NB}})$, where RCG_NB refers to the combination of boxy bulge and nuclear bulge.

Robust results can only be obtained if they do not critically depend on the choices made. To test this, we increase or decrease the allowed range of the spatial or spectral nuisance parameters by a factor four, for each of the diffuse (the ICS component plus the three gas rings) components separately, as well as for the 3FGL sources. We find that the preference for the RCG+NB model over the Einasto model is rather stable under changes. More specifically, the

$\Delta\chi^2$ changes to 364 (72) when the spatial nuisance parameter range of the outer gas ring is increased (decreased) by a factor of 4. In all other cases, the variation is smaller. We checked that the inferred best-fit spectra for the RCG and NB components does not vary by more than 30% or a factor of two, respectively. We also checked that increasing the spectral freedom of the three gas rings or the ICS component individually has no noticeable effect on our results.

B.3. Relevance of the size of the ROI

We find that the large ROI that we use in our analysis ($|b| < 20^\circ$ and $|\ell| < 90^\circ$) plays an important role for obtaining robust and stable results. The central point is that the best discriminator for the various diffuse model components is their spatial extent along the Galactic plane and towards high latitudes. This discriminator is lost if the analysis is limited to a too-small ROI. Instead, the results start then to depend on specific small-scale shape differences between the components, which are usually hard to model and susceptible to a large range of systematic uncertainties. This becomes particularly problematic if the signal of interest has the same spatial extent as the ROI.

For instance, the different gas components overlap in the inner Galaxy along the Galactic disk (say, $|b| < 5^\circ$, $|\ell| < 20^\circ$), and are hard to discriminate in a fit that is limited to an ROI of comparable size. However, the various components differ – by construction – in their longitudinal extent. Including a larger portion of the Galactic disk, as we do in our analysis, provides enough leverage to disentangle the components and constrain their energy spectrum and normalization. At the same time, the modulation parameters that we introduced in our analysis allow to account for inaccuracies of the modeled components at smaller scales. A similar argument holds for our treatment of the Fermi bubbles (see Sec. B.4) and ICS emission.

The X-shaped bulge.— The above effects explain why we can not confirm the recent claims by [Macias et al. \(2016\)](#) that the GCE is best described by an X-shaped bulge template. In fact, we find that we can reproduce the results from this paper if we (a) restrict our analysis to the same ROI (a $15^\circ \times 15^\circ$ region around the GC), (b) allow complete spectral freedom and (c) fix the spatial templates. Under these conditions, we find indeed that the X-shaped bulge is preferred over the RCG+NB template, with a similar best-fit spectrum as shown in [Macias et al. \(2016\)](#). However, from our analysis it appears that most of the emission previously attributed to the GCE is *falsely* absorbed by the gas templates when using the smaller ROI. We find that such a fit leads to results inconsistent with the data as soon as one increases the size of the ROI.

One might argue that a small ROI should lead to more robust results, by increasing statistical error bars and making the results less dependent on a mismodeling of diffuse Galactic emission at large scales. However, this is only strictly true if the shape of all model components is accurately known. Mismodeling will introduce biases, which play an increasingly large role if the most prominent differences between the signal of interest and the background components are removed by using a small ROI.

A potential caveat when comparing to the results of [Macias et al. \(2016\)](#) is that they apply newly developed hydrodynamical gas maps which they find to be highly preferred over the interpolated gas maps we use in our analysis. However, since we are able to reproduce their main results also when using interpolated gas maps, namely a preference for an X-shaped bulge with a similar spectrum as found in [Macias et al. \(2016\)](#), we do not expect the hydrodynamical gas maps to be driving the preference for an X-shaped component. Rather, we find that when connecting our analysis to theirs the smaller ROI drives the difference, which as argued above leads to inconsistencies when extrapolating the templates outside of their fit region.

B.4. Fermi bubbles and the role of star formation in the CMZ

Using H.E.S.S. and *Fermi*-LAT data, [Jouvin et al. \(2017\)](#) estimate the supernova recurrence time in the CMZ to be ~ 2500 yrs. Assuming 10% of the kinetic energy goes into cosmic rays, and 1% into electrons, this corresponds to an average injection of $\sim 10^{37}$ erg s $^{-1}$ into cosmic-ray electrons. This is comparable to the luminosity of the GCE component in our fits ($\sim 1.7 \times 10^{37}$ erg s $^{-1}$). However, it is generally expected that a fraction of the electron cosmic-ray energy is lost at radio frequencies by synchrotron radiation. Furthermore, the expected γ -ray spectrum would be most likely hard, comparable to the *Fermi* Bubbles spectrum or the spectrum of our ICS template. In our analysis, we expect that this component manifests as low-latitude component of the *Fermi* Bubbles. Interestingly, we find that total luminosity of our low-latitude *Fermi* Bubbles component is $\sim 3.6 \times 10^{36}$ erg s $^{-1}$ (for a $10^\circ \times 10^\circ$ ROI around the GC integrated over all energies, run `r5.RCG_NB`). A possible connection to star formation in the CMZ will be explored elsewhere.

The spectrum of the GCE differs significantly from the high-latitude *Fermi* Bubbles spectrum (e.g. [Huang et al. 2016](#)). However, the emission that should be associated with the *Fermi* Bubbles at low energies is unknown. We

test the robustness of our results against different *Fermi* Bubbles characterizations. For this purpose we reanalyze `r5_RCG_NB` with a hardened/softened bubble spectrum, by multiplying its original spectrum by a power law of $E^{\pm 0.05}$ (`r5_RCG_NB_±GeV`). As seen in Fig. 6, the spectra of the RCG and NB components are very similar to those in the run with the original bubble spectrum, changing by less than 20%. In addition, as discussed in Section B.1, we implemented a fixed uniform morphology for the *Fermi* Bubbles as in Calore et al. (2015b), in which case the GCE component is increased by $\sim 20\%$. Lastly, test models where we allow an additional spectral component in the inner $10^\circ \times 10^\circ$ region of the Galactic center, with completely free morphology, and a spectrum either fixed to the ICS component of our main runs (which is significantly softer than the *Fermi* Bubbles spectrum), or to the spectrum of the *Fermi* Bubbles multiplied by $E^{0.1}$, which is significantly harder. In the first case (`r5_GCE_NB_pICS`), this component does not pick up a significant amount of the inner Galaxy emission, but in the second case (`r5_GCE_NB_pICS2`) it absorbs much of the enhanced bubble emission that we see in our main runs. In both cases, the GCE flux is not affected much (the RCG component by less than 20%, the NB is barely affected). This suggests that the freedom introduced with of our *Fermi* Bubbles template is already enough to account, together with the GCE, for most of the inner Galaxy emission.

B.5. The role of point sources

A recent dedicated search for point sources in the inner Galaxy was performed by the Fermi Collaboration and resulted in the publication of the 2FIG catalog (Ajello et al. 2017). We test the effect of including these additional sources on the GCE in our runs by including all 2FIG sources that are not in the 3FGL catalog and not found in clusters near other known point or extended sources. The spectra and positions are taken from the 2FIG catalog and the same modulation parameters as for the 3FGL sources are used. We find that the adding the 2FIG sources does not change the preference for the RCG+NB templates over the DM templates. The RCG+NB template is still preferred over the Einasto profile by a $\Delta\chi^2 > 100$. The GCE fluxes are reduced by $< 5\%$ to 15% at most when including the 2FIG sources. The one exception is the X-shaped template; the flux of this template is reduced by 50% . However, this component is already so sub-dominant it has little effect on the overall quality of the fit.